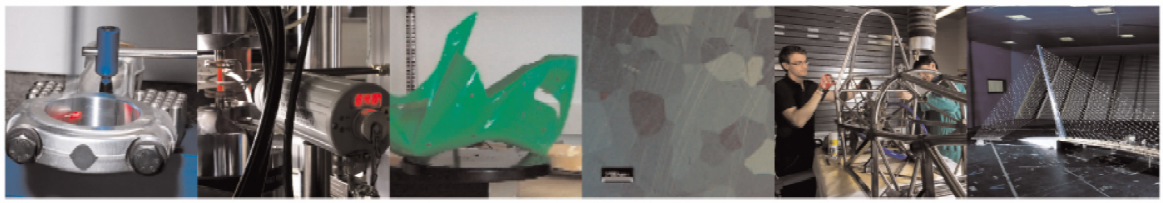

Nonintrusive estimation of subsurface geometrical attributes of the melt pool through the sensing of surface oscillations in laser powder bed fusion

Caprio, Leonardo; Demir, Ali Gökhan; Previtali, Barbara

Non-intrusive estimation of sub-surface geometrical attributes of the melt pool through the sensing of surface oscillations in laser powder bed fusion

Leonardo Caprio[1], Ali Gökhan Demir[1], Barbara Previtali[1]

[1] Department of Mechanical Engineering, Politecnico di Milano, Via Giuseppe La Masa 1, 20156 Milan, Italy

Abstract

Molten pool geometry, whose surface parameters may be extrapolated through direct process observations, has been identified as a fundamental indicator of stability in Laser Powder Bed Fusion (LPBF). However, a parameter which cannot be directly measured on industrial systems by means of conventional sensing equipment is the molten pool depth. Indeed, methods based on X-ray imaging demonstrated in literature have helped a better understanding of the process. However, retrofitting such solutions to industrial systems does not appear as a viable route currently. Within the present investigation, a non-intrusive sensing method for the indirect measurement of sub-surface molten pool geometry based upon the detection of surface oscillations is presented. The analysis of frames acquired using a high speed camera and a secondary illumination light allows the identification of the crests of molten pool capillary waves through bright reflections on the surface of the molten pool. The characteristic oscillation frequency of the surface ripples may be correlated to penetration depth or to other sub-surface geometrical parameters.

Proof of concept testing of the sensing principle was conducted on two different materials, namely AISI316L and IN718, by means of single track LPBF depositions. Experiments were conducted at different levels of laser emission power to induce variations in molten pool characteristics. The process was observed employing an off-axis illumination light and a high-speed camera, which allowed acquisitions with high spatial and temporal resolution. The acquired frames were post-processed to extract the oscillation indicator and analysis of the Power Spectral Density of the signal allowed to identify the oscillation frequency.

Results show that oscillation frequencies range from 3 to 5.5 kHz. Molten pool penetration depth and cross-sectional area could be correlated to the oscillation frequencies for the in-line detection of these parameters during LPBF depositions. For both materials, higher oscillation frequencies corresponded to shallower molten pool and smaller mass of molten material. Moreover, different characteristic curves of oscillation frequency variations as a function of the melt pool cross-sectional area were determined for IN718 and AISI316L.

Keywords: laser powder bed fusion, oscillation, high speed imaging, melt pool, monitoring

Introduction

In LPBF the machine architecture and the layer-by-layer build-up nature of the process allow for *in-situ* monitoring and in-line qualification of the built parts [1,2]. A wide part of the scientific community has been investigating optical emission monitoring on the powder bed surface to detect different molten pool characteristics, such as surface temperature and geometry, which may be considered as process stability indicators. Craeghs *et al.* have shown how the detection of melt pool geometrical features may be effective to avoid process drifts[3,4]. Demir *et al.* have shown how molten pool area may be used to avoid the formation of overheated regions [5]. Vasileska *et al.* exploited these measurements for a layer-wise LPBF closed-loop control scheme [6]. Thermal camera imaging has been employed to determine temperature distributions and cooling rates in the LPBF process [7]. Spatially distributed molten pool temperatures have also been detected by combining of two high-speed cameras and observing the process at different wavelengths [8]. On the other hand pyrometers may be employed to retrieve melt pool temperatures at elevated acquisition rates (>50 kHz) whilst loosing spatially resolved data [9,10].

The various process information collected using different sensors has been employed for phenomenological studies to promote the understanding of fundamental process physics as well as the development of monitoring devices which may be implemented onto industrial systems. One key aspect regards the melt pool depth, which essentially requires transmissive imaging techniques for a direct geometrical observation. Recently, X-ray transmission imaging techniques allowed to observe molten pool dynamics and penetration depth during the LPBF process [11–13]. These detection methods allowed for unprecedented observation of molten pool morphology in LPBF, providing

observations of the missing third dimension (i.e. the molten pool depth). However, the adaptation of such monitoring devices onto industrial machines results technically unfeasible. It is thus of interest for the scientific and industrial communities to develop a sensing approach capable of providing information related to sub-surface molten pool geometry in a non-intrusive and economically convenient way.

The measurement of penetration depth and melt pool geometry is a topic which has been extensively investigated for the Gas Tungsten Arc (GTA) welding process. The first studies related to the topic date back to the 1980s and investigations continued throughout the years [14–16]. These sensing approaches rely on the correlation between the surface oscillations of the molten pool and its geometry, exploiting such information to determine when partially or fully penetrated welds are obtained. Both empirical (see Renwick and Richardson [14]) and analytical models (as in the works by Sorensen and Eagar, Xiao and Den Ouden, Yoo and Richardson[17–19]) have been built to depict the relationship between surface capillary waves and penetration depth or molten pool cross-sectional area. Experimental approaches mostly rely on the measurement of the arc voltage, an inherently available sensing system of the GTA welding technology.

Clearly, the use of the arc voltage may not be employed for laser based processing. However, similar process indicators may be sought for the detection of surface oscillations whilst still exploiting the correlation between such capillary oscillations and the sub-surface melt pool geometrical attributes. For instance Semak *et al.* demonstrated that using a secondary probe light and a photomultiplier, it is possible to measure surface oscillations during laser welding experiments [20]. Capillary wave oscillations have been also been detected in the LPBF process by Richter *et al.* through analysis of high speed X-ray transmission imaging [21].

The aim of the present work is to demonstrate that a sensing system based on the detection of surface oscillations by means of a secondary illumination light can be employed to estimate sub-surface geometrical attributes. Proof of concept demonstration of this approach for the LPBF process was conducted by observing single track depositions via an off-axis high speed camera and a secondary illumination light. The probe light allowed to both suppress the process emission and highlight the crests of the capillary surface waves through their bright reflections. Hence, it was possible to extrapolate oscillation frequencies through image and signal analysis. Results are reported and correlated to the cross-sectional geometry of the melt for two different materials, AISI316L and IN718. Finally, a discussion regarding the melting behaviour of the different materials in the various processing conditions concludes the article.

Materials and method

Materials

For the present investigation, gas atomized metallic powders were employed for the LPBF single track depositions. The AISI316L powder was supplied by Cogne Acciai (Brescia, Italy) with a granulometry comprised between 15 to 45 μm and chemical composition as indicated in Table 1.

Table 1. Chemical composition of AISI316L powder

Elem	Fe	Ni	Cr	Mo	C	Si	Mn	P	S
wt%	Bal	11.4	17.3	2.46	0.02	0.52	1.5	0.01	0.007

The IN718 gas atomized powder was provided by LPW (Runcorn, United Kingdom) with a granulometry comprised between 18 and 47 μm and chemical composition shown in Table 2. Baseplates of respectively corresponding chemical composition were employed for the single track LPBF tests. A 12 mm thick base plate was used for the AISI316L deposition whereas a 3 mm thick baseplate was employed for the IN718 depositions.

Table 2. Chemical composition of IN718 powder

Elem	Fe	Ni	Cr	Mo	C	Ti	Nb+Ta	N	O
wt%	18.2	Bal	19.0	2.98	0.03	0.97	5.16	0.01	0.02

Laser system and optical chain

A 1 kW single mode fiber laser was employed as the light source (nLight Alta, nLight, Vancouver, WA, USA). The beam trajectories were designed employing Scan Master Designer software (Cambridge Technologies, Bedford, MA).

The laser was deflected onto the work area by means of a scanner head (Smart Scan, Smart Move GmbH, Garching bei München, Germany) and focused to the waist diameter by means of a 420 mm F-Theta lens.

Table 3. Specifications of the laser system

Parameter	Value
Emission wavelength, λ (nm)	1080
Beam quality factor, M^2	1.19
Beam waist diameter, d_0 (μm)	78
Max. laser power, P_{max} (W)	1000

The theoretical beam waist diameter on the focal plane was d_0 = 78 μm. The main specifications of laser system and optical chain are reported in Table 3.

Laser Powder Bed Fusion system

A prototype LPBF system was employed for the powder delivery and substrate positioning. The open architecture of the LPBF machine allowed for the flexible adaptation of the optical monitoring system and baseplates [22,23]. In the present experiments the system was equipped with a nozzle for localized gas supply in the laser-material interaction area. A fan was also employed to protect the scanner head and the high speed imaging equipment by blowing away the process debris.

High speed imaging equipment

A high-speed camera and a secondary illumination light were employed to observe the process from an off-axis perspective. The illumination light was a CAVILUX HF (Cavitar, Tampere, Finland) laser source emitting at 640 nm synchronized with the shutter of the camera. The high-speed camera equipped with a CMOS sensor was a Fastcam Mini AX200 (Photron, Tokyo) equipped with optics enabling elevated spatial resolution. The active sensor region could be flexibly modified and was set to 1024 x 240 pixels in order to achieve an acquisition frequency of 25 000 Hz. Details of the high speed imaging (HSI) set up are reported also in Table 4.

Table 4. Specifications of the HSI system

Specification	Value
Monitoring configuration	Off-axis
Observation wavelength, λ_{obs} (nm)	640
Acquisition frequency, f_{acq} (Hz)	25 000
Spatial resolution, *SR* (μm/pixel)	4
Field of view, *FOV* (pixel x pixel)	1024 x 240
Field of view (mm x mm)	4.096 x 0.96

Experimental design

The overall experimental set up with the laser system, mechanical powder deposition and monitoring equipment for the single track LPBF depositions is shown in Figure 1. Argon was employed as local shielding gas and the observation configuration was maintained identical for all experimental conditions. The high speed camera inclination had a zenith angle lower than 30° in order to obtain a top-view of the molten pool with the lowest distortion possible. Experiments were planned at a fixed value of scan speed (v_s= 100 mm/s) and at constant layer thickness corresponding to t=50 μm. The single track powder bed fusion experiments were conducted at three levels of laser power, *P* ranging from 200 W to 300 W. The LPBF single track depositions were conducted with a combination of powder and baseplate respectively of AISI316L and IN718.

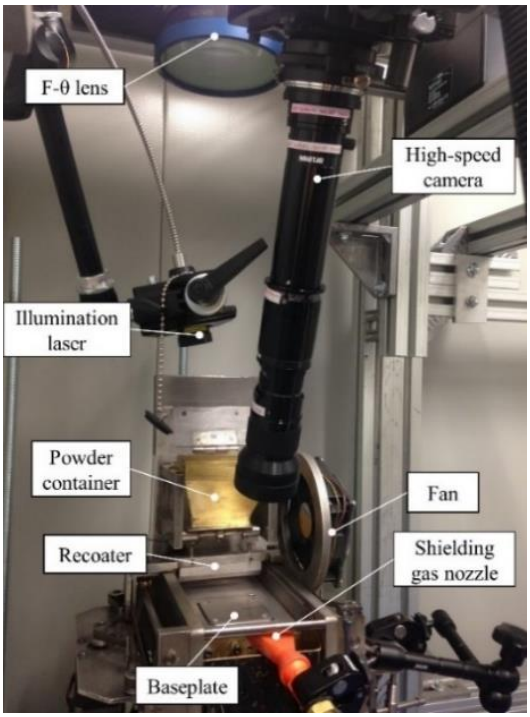

Figure 1. Off-axis high-speed imaging set-up mounted on the open architecture LPBF system

Every experimental condition was replicated twice (i.e. two single track depositions were monitored per each combination of process parameters and material configuration). The fixed and variable factors of the experimental plan are reported in Table 5.

Table 5. Fixed and variable factors of the experimental plan for the proof of concept testing

Fixed factors	
Process gas	Argon
Scan speed, v_s (mm/s)	100
Layer thickness, t (μm)	50
Focal position, h_f(mm)	0
Variable factors	
Laser power, P (W)	200 – 250 – 300
Material	AISI316L – IN718

Image processing

Following the HSI acquisitions, image processing of the video frames was conducted in order to identify the molten pool. Melt pool identification was obtained through a self-developed algorithm in Matlab environment. First, background removal was achieved by subtracting successive frames. Further image processing steps were applied in order to denoise the acquired image and correctly identify the molten pool outer boundaries (these are not reported in the text for brevity). Once the molten pool was identified a region of interest (ROI) for the detection of the bright reflections was defined starting from the melt pool front coordinate. A sample frame of the molten pool outline and selected ROI are shown in Figure 2

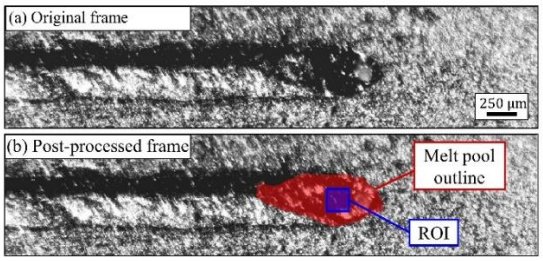

Figure 2. Sample frame from HSI acquisition of single track LPBF deposition of IN718: (a) Original frame and (b) post-processed frame for feature extraction

A square ROI of 40 x 40 pixels ($N_{pix,ROI}$) was positioned from the molten pool front at a distance corresponding to 0.75 of the molten pool average width. The location of the region of interest was chosen in this position since the main swelling region of the molten pool is located just behind the laser material interaction area as indicated by Fabbro [24]. This area can thus be considered to correspond to a position with the greater oscillation amplitudes.

Hence, by analyzing the periodicity of bright reflections within this region it is possible to identify principal oscillation frequency of the molten pool. The following intensity indicator $I_{sum,ROI}$ could be identified as:

$$I_{sum,ROI} = \sum_{i=1}^{N_{pix,ROI}} I_i \tag{1}$$

where I_i is the intensity of the *i*-th pixel and the summation operates for all the pixels belonging to the region of interest.

Signal processing

Measuring $I_{sum,ROI}$ for every time instant generates a time varying signal. To identify the principal frequency of such a signal requires the estimation of the Power Spectral Density (PSD). In order to have a consistent estimate of such parameter, different approaches may be employed (for instance Bartlett's method or Welch's method with different spectral windows)[25]. However, there is evidence that multi-taper spectral estimation, as defined by Thomson, outperforms other methods [26]. Thomson's multi-taper estimate of the PSD was thus computed within Matlab environment by means of the *pmtm.m* function. The acquired signals were not zero-padded in order to avoid introducing bias in the spectral density estimate. A fundamental parameter, which affects the number of tapers employed by Thomson's method and thus the leakage error of the spectral domain analysis, is the time-to-bandwidth parameter *TBW*. This parameter relates the acquisition time, T_{acq} and the narrow bandwidth frequency resolution of the spectral estimate, Δf_{res} according to the following relationship[27]:

$$TBW = \frac{T_{acq} \cdot \Delta f_{res}}{2} \tag{2}$$

Given a certain scan speed and a fixed field of view whose length is l_{FOV} the acquisition time of signal is determined as follows:

$$T_{acq} = \frac{l_{FOV} - l_{mp}}{v_s} \tag{3}$$

where l_{mp} refers to the melt pool length and penalizes the acquisition time due to the need of having a complete melt pool within the acquired frame. Hence, by combining Equations 2 and 3 it is possible to estimate the frequency resolution as follows:

$$\Delta f_{res} = \frac{2 \cdot TBW \cdot v_s}{l_{FOV} - l_{mp}} \tag{4}$$

As the *TBW* parameter increases there is a loss in the narrow-bandwidth resolution of the spectral estimate although the confidence interval of the estimate is reduced [26]. In the literature of molten pool oscillations, often a single oscillation peak is measured (whereas higher order contributions are often damped)[18]. Moreover, in the case of more than one oscillation peak these are often distanced by several hundreds, if not thousands, of hertz [28]. Given that molten pool length for the AISI316L, LPBF process has been observed to be in the order of 1-1.5 mm [29,30] and considering the *FOV* chosen for the present experimentation, a time-to-bandwidth parameter *TBW*=6 was selected. The frequency resolution was Δf_{res}= 462 Hz.

Metallographic characterization

In order to expose the sub-surface molten pool geometry, the single track LPBF depositions were cut transversally to the laser scanning direction. The surface of the cross-sections was prepared for metallographic analysis through polishing and chemical etching. Etching solution for AISI316L consisted in 1ml of nitric acid 65% concentration, 1ml of chloridic acid 37% concentration and 1ml of water , whilst for IN718 a solution composed by 1g $CuCl_2$, 8 ml of HCl, 5 ml of ethanol and 6 ml of H_20 was employed. For each single track, four cross-sections were exposed. Image analysis allowed to measure melt pool cross-sectional area (A_{cs}) and penetration depth (h).

Results

Off-axis high-speed imaging acquisitions

The high speed imaging observations of both the AISI316L and IN718 single track depositions exhibited the presence of bright reflections on the molten pool surface (as visible from the sample frames shown in Figure 3). These motion of these reflections indicated the dynamics of the molten pool although from qualitative analysis of the latter it was not possible to make any inference. On the other hand, the high speed imaging algorithm allowed to retrieve the molten pool contour for every frame and successfully extract the $I_{sum,ROI}$ indicator for the successive analysis.

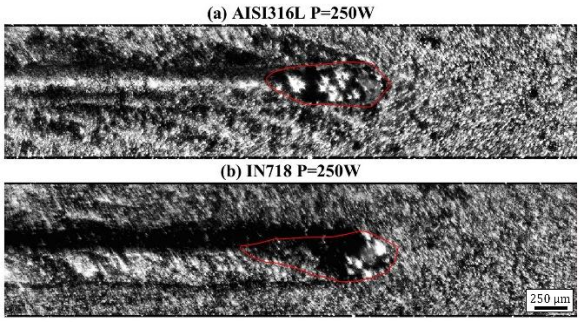

Figure 3. Sample frames from the HSI acquisitions of single track LPBF depositions of (a) AISI316L and (b) IN718. Red line indicates melt pool outline.

In all processing conditions, at constant level of emission power, the IN718 molten pool exhibited a larger and longer molten pool with respect to the AISI 316L (quantitative measurements of the molten pool from the HSI acquisitions are not reported for brevity).

Metallographic cross-sections

According to the geometrical criteria proposed by King *et al.* [31], the morphological analysis of the melt geometry in the sample cross-sections reported in Figure 4 evidences in all the process conditions the keyhole formation. Although standard LPBF processing conditions tend to avoid keyhole formation, at a level of proof of concept testing the conditions can be acceptable to reveal the feasibility of the proposed approach.

Coupling the high speed imaging observations with the melt cross-sectional morphology it is possible to note that in both cases the IN718 melt pool exhibited a larger width. On the other hand, penetration depth does not appear to show significant differences between the IN718 and AISI316L depositions.

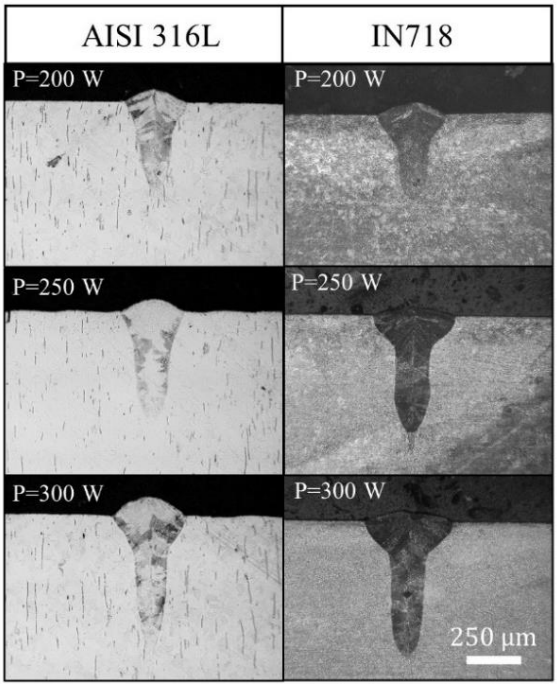

Figure 4. Metallographic cross-sections of single track LPBF deposition of AISI316L and IN718 at different levels of emission power.

Quantitative measurements of the penetration depth are reported in Figure 5(a) and indicate no statistical difference between the two materials. Contrarily, the difference in molten pool width between IN718 and AISI316L depositions are observable both through the high speed images and the metallographic cross-sections. The width measurements are shown in Figure 5(b). Cross-sectional area may be considered as representative of the mass of molten material and thus found as a fundamental factor which affects molten pool oscillations [32]. Coherently, with previous work by Fabbro, the molten pool depth in keyhole processing mode shows a linear increase with increasing levels of laser power. [24].

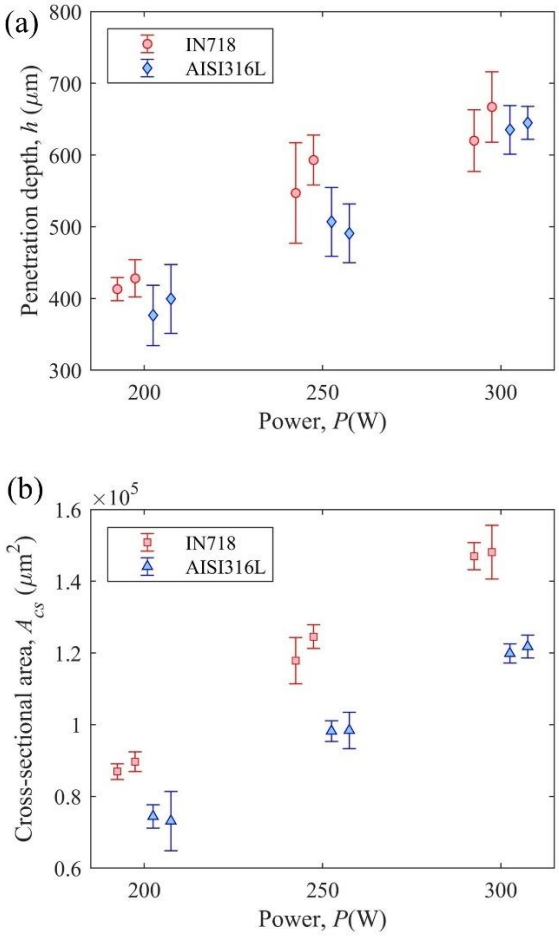

Figure 5. Interval plot for (a) penetration depth and (b) cross-sectional area of the melt pool for all the experimental conditions and replicates. Error bars are one standard deviation from the mean. Results for IN718 in red, AISI316L in blue.

Melt pool oscillation frequencies

Analysis in the frequency domain according to the previously presented methodology, allowed to estimate the Power Spectral Density (PSD) of the $I_{sum,ROI}$ indicator for every experimental condition. Figure 6 shows the results for the AISI316L depositions whilst Figure 7 reports the PSD for the IN718 tests. The principal oscillation frequency of the various conditions is obtained through the identification of the strongest peak, which could be simply achieved by determining the absolute maximum of the PSD estimate. A circular marker is added to the PSD plots to identify the peak position which corresponds to the principal oscillation frequency.

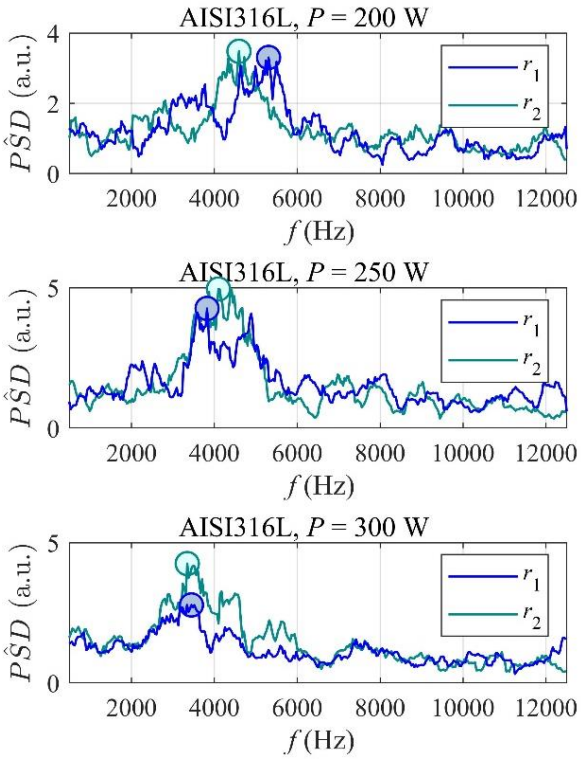

Figure 6. PSD for single track LPBF depositions of AISI316L. Replicates in different colours, oscillation frequency indicated by circular marker.

The signal energy distribution clearly indicates the oscillation frequency for both AISI316L and IN718. The main oscillation frequency for both materials were identified in the range of 3 to 5.5 kHz which is consistent with the measurements of Richter *et al.* for the LPBF processing of CoCr alloy [21]. At lower levels of emission power the capillary waves oscillate at higher frequencies as can be clearly viewed by the position of the oscillation peaks of Figure 6 and Figure 7.

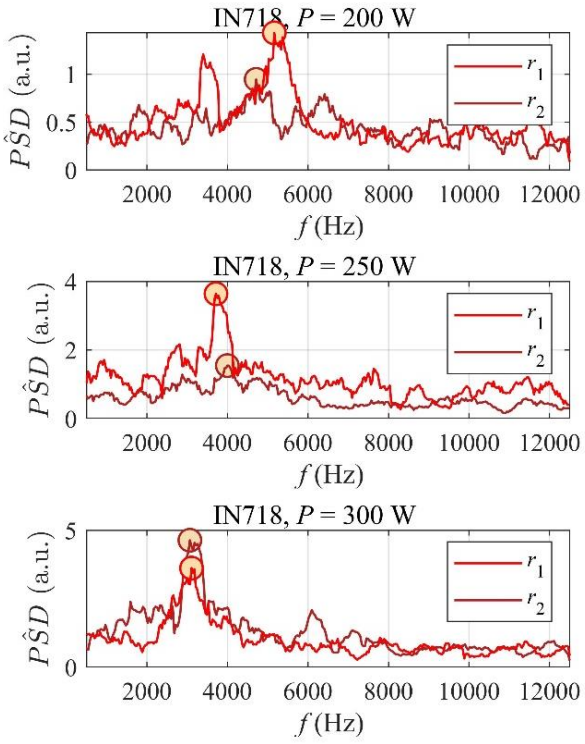

Figure 7. PSD for single track LPBF depositions of IN718. Replicates in different colours, oscillation frequency indicated by circular marker.

Analysis of variance (ANOVA) was conducted on the results. The interval plot shown in Figure 8 clearly indicates the influence of the laser emission power on the measured variable. On the other hand, the type of material processed does not appear to influence the oscillation frequency of the molten pool.

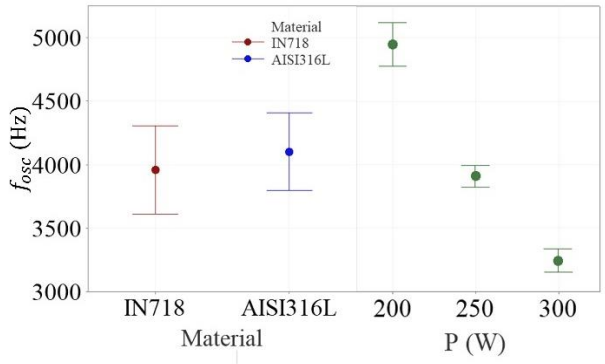

Figure 8. Interval plot of oscillation frequency as a function of laser power and processed material. Error bars are one standard error from the mean

The results of ANOVA shown in Table 6, confirm the indication of the interval plot in Figure 8. The material is not statistically significant for the oscillation frequency whilst the laser emission power with a statistical significance value at α=0.05. The statistical model shows a good agreement with an R^2_{adj} value of 89.61 %. The non-significance of the material in determining the oscillation may be linked to the fact that IN718 and AISI316L exhibit similar physical properties during processing, which is discussed in the following sections.

Table 6. ANOVA table for oscillation frequency f_{osc}

Source	DF	Adj SS	Adj MS	F-Value	P-Value
P (W)	2	5885958	2942979	48.42	0.000
Material	1	60148	60148	0.99	0.349
Error	8	486204	60775		

Lack-of-Fit		2	45987	22993	0.31	0.742
Pure Error		6	440217	73370		
Total		11	6432310			

Model summary

S	R^2	R^2 (adj)	R^2(pred)
246.527	92.44%	89.61%	82.99%

Oscillation frequency to sub-surface geometrical parameter correlation

The melt pool oscillation frequencies extrapolated through the high speed imaging acquisitions may be correlated to the sub-surface geometrical parameters: penetration depth and cross-sectional area. In Figure 9 (a) and (b) the data is reported graphically alongside with the fitted trend curves. From the graphical representations it is possible to view how an increase in oscillation frequency is symptomatic of a reduced penetration depth. Analogously, as the cross-sectional area decreases the oscillation frequencies according to a relationship of the type $A_{cs} \propto {}^{1}/_{f_{osc}}$.

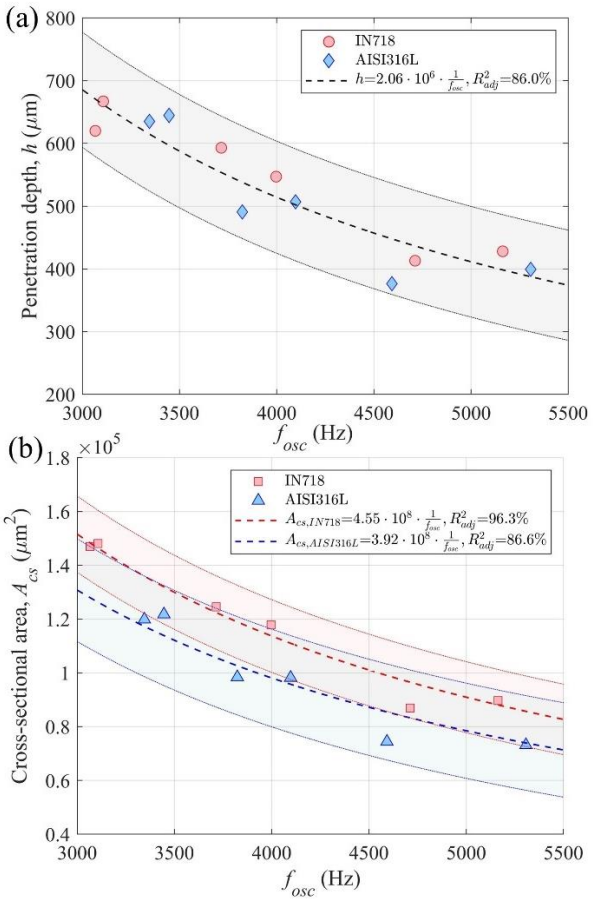

Figure 9. (a) Melt pool penetration depth, h against oscillation frequency f_{osc} and (b) cross-sectional area A_{cs} against oscillation frequency, f_{osc}. Data points for IN718 in red, for AISI316L in blue. Regression equations are presented in dashed lines. Coloured bands show the prediction intervals.

Discussion

The results of the present work show that a correlation between molten pool surface oscillations and penetration depth exists, and that the monitoring solution may be employed to determine liquid surface fluctuations. On the other hand, the sensing approach exhibits limitations and the need for further comprehension of the underlying physical phenomena. The influence of the laser emission power is clearly a major factor in establishing the penetration depth of the single tracks (a greater energetic input corresponds to a higher penetration depth). However, the non-significance of type of material on the oscillation frequency opens the way for discussion.

Analytical models determine the oscillation frequency of the molten pool as proportional to the ratio between surface tension γ and material density in liquid state ρ_L. In literature this relationship has been often indicated according to the following formulation [17,33]:

$$f_{th} = \frac{1}{2\pi}\sqrt{\left(gn + \frac{\gamma}{\rho_L}n^3\right)} \quad (5)$$

where *g* refers to gravitational acceleration and *n* refers to the wavenumber of the oscillation. As a matter of fact, for purely capillary waves the contribution of the gravitational term may be neglected as has been done in previous investigations [33]. AISI316L and IN718 exhibit similar characteristics in terms of the surface tension to density parameter (as reported in Table 8 the Appendix section). Hence, the oscillation modes of the system may be considered analogous. However, this model describes the mechanical system characteristics of the liquid metal pool but does not take into account the effect of a forcing input to the system.

At high power density *PD* levels there is the onset of material vaporization and plasma ionization. The threshold value at which the phenomenon occurs is in the order of $1 \cdot 10^6$ W/cm^2 and it has been shown that vapor depression formation always occurs in standard LPBF processing conditions and is independent of the laser scanning velocity[34]. The power density may be calculated as the ratio between the laser power and the area of the beam spot:

$$PD = \frac{4 \cdot P}{\pi d_0^2} \quad (6)$$

The *PD* for the present investigation was always in excess of $4 \cdot 10^6$ W/cm^2 hence implying that vapor depression and with such plasma formation was always present. Under these circumstances, the recoil force generated by the ionized material may be considered as one of the dominant forces acting upon the molten metal. Considering the similar chemical composition and laser absorptivity of the materials, AISI316L and IN718 are expected to behave analogous from an ionization perspective. Hence, the similar behavior in terms of molten pool fluctuations may be reconnected to the vapor-induced oscillations. Certainly, further investigations supported by a larger data set of experiments and process modelling are required to achieve a deeper understanding but these are the preliminary indications retrieved from the present results.

A last aspect worth discussing are the differences in the molten pool cross-sectional area and morphology between the AISI316L and IN718 tracks. Two distinct correlation curves could be determined for oscillation frequency variations with respect to the cross-sectional area of the IN718 and AISI316L single track LPBF depositions. These may be explained by the greater amount of material melted during the processing of the IN718 tracks with the same process parameters.

Since keyhole formation conditions were denoted during the processing of both materials, it is possible to compare their thermal response assuming an equally absorbed laser power. Laser absorptivity greatly increases in keyhole processing mode, tending to a fixed value comparable for the two materials [35,36]. Moreover, powder bed absorptivity for AISI316L and IN718 is analogous (values reported in Table 7)[37].

Table 7. Tabulated physical properties of AISI316L and IN718 [37,38].

Material property	AISI316L	IN718
Surface tension, γ (N/m)	1.7	1.88
Density at $T=T_L$, ρ_L (kg/m^3)	6880	7033
Density at $T=T_{amb}$, ρ_{amb} (kg/m^3)	7950	8190
Specific heat capacity, c_p (J/kgK)	470	435
Thermal conductivity, κ (W/mK)	13.4	10
Latent heat of fusion, L_f (kJ/kg)	260	210
Solidus temperature, T_S (°C)	1385	1260
Liquidus temperature, T_L (°C)	1450	1336
Absorptivity at λ=1 μm, a	69.91	69.29

Volumetric melting enthalpy H_m may be viewed as the specific energy required to melt a material during LPBF processing[39]:

$$H_m = \rho_{amb}(c_p \cdot (T_S - T_{amb}) + L_f) \tag{7}$$

where ρ_{amb} is the material density at ambient temperature, c_p the specific heat capacity and T_S the solidus temperature of the material. Calculated values for this parameter are reported in Table 8. Interestingly enough, IN718 exhibits a lower value of H_m when compared to AISI316L as well as a lower latent heat of fusion L_f. Hence, the greater cross-sectional area of the IN718 tracks with respect to AISI316L depositions is representative of the greater mass of material melted due to the lower specific energetic input required by the nickel based alloy (given a fixed input power).

In order, to explain the different melt pool morphology of the two materials, it is possible to refer to the thermal diffusivity parameter which regulates the heat transfer mechanisms during the processing of materials by concentrated heat sources.

Table 8. Calculated physical properties of AISI316L and IN718

Material property	AISI316L	IN718
Surface tension to density ratio, γ/ρ (m^3/s^2)	$2.47 \cdot 10^{-4}$	$2.68 \cdot 10^{-4}$
Thermal diffusivity, α (m^2/s)	$3.6 \cdot 10^{-6}$	$2.5 \cdot 10^{-6}$
Volumetric melting enthalpy, H_m (J/m^3)	$5.42 \cdot 10^{9}$	$4.76 \cdot 10^{9}$

Thermal diffusivity α, is determined as the ratio between the thermal conductivity and the product of the material density at ambient temperature ρ_{amb} and specific heat capacity c_p [39]:

$$\alpha = \frac{\kappa}{\rho_{amb} \cdot c_p} \tag{8}$$

Values of the calculated thermal diffusivity for the two materials are reported in Table 8. Lower values of thermal diffusivity, at constant energetic input imply that heat transfer in the transverse direction with respect to laser incident trajectory will tend to be reduced as in the case of the AISI316L depositions. In fact, the melt pool penetration depth of the stainless steel depositions is comparable to that of IN718 although track width is reduced due to $\alpha_{AISI316L} > \alpha_{IN718}$. Future investigations should attempt at validating the process and indicating if a link between the melt pool morphology and oscillation response to a forced input is significant. According to the present results, this aspect appears to be a second order effect.

Conclusions

This work presents a non-intrusive measurement system which allows to estimate the sub-surface geometrical attributes of the molten pool in the LPBF process through oscillation frequency identification of the capillary surface waves. The measurement is conducted through a sensing device based on the use of high speed imaging equipment and a secondary illumination light. The methodological approach for the oscillation frequency identification by means of image and signal processing is presented.

The sensing principle was validated by conducting experiments on two different materials namely IN718 and AISI316L commonly processed by LPBF. Results show that a correlation could be established between the oscillation frequencies, penetration depth and cross-sectional area. Higher oscillation frequencies corresponded to shallower molten pools with a smaller mass of molten material.

The two materials showed similar correlations between the capillary oscillations and the geometrical attributes although different characteristic curves could be asserted. These discrepancies may be reconducted to the different physical properties of the material. The higher melting enthalpy and thermal diffusivity of AISI316L yields single track depositions with smaller cross-sectional area with respect to IN718 but with comparable values in terms of penetration depth and oscillation frequencies.

Future developments of the system should consider its coaxial implementation and downsizing in terms of costs of the hardware and data transfer rate to ensure industrial applicability.

Acknowledgments

The authors would like to thank nLight for providing the laser source for the off-axis monitoring experiments. Acknowledgments also go to Optoprim Srl for providing the scanner head and the controller card for the off-axis experiments. The Italian Ministry of Education, University and Research is acknowledged for the support provided through the Project "Department of Excellence LIS4.0 - Lightweight and Smart Structures for Industry 4.0". The authors are grateful to Adige S.p.A. of the BLM Group for providing the high speed imaging equipment. The project presented in this paper has been funded with the contribution of the Autonomous Province of Trento, Italy, through the Regional Law 6/98 (Project LT 4.0).

References

[1] Grasso M, Colosimo BM. Process defects and *in situ* monitoring methods in metal powder bed fusion: a review. Meas Sci Technol. (2017)28(4):044005.

[2] Everton SK, Hirsch M, Stravroulakis P, Leach RK, Clare AT, Stavroulakis PI, et al. Review of in-situ process monitoring and in-situ metrology for metal additive manufacturing. Mater Des. (2016)95:431–45.

[3] Craeghs T, Clijsters S, Yasa E, Bechmann F, Berumen S, Kruth J. Determination of geometrical factors in Layerwise Laser Melting using optical process monitoring. Opt Lasers Eng. (2011)49(12):1440–6.

[4] Craeghs T, Bechmann F, Berumen S, Kruth JP. Feedback control of Layerwise Laser Melting using optical sensors. Phys Procedia. (2010)5(PART 2):505–14.

[5] Demir AG, Mazzoleni L, Caprio L, Pacher M, Previtali B. Complementary use of pulsed and continuous wave emission modes to stabilize melt pool geometry in laser powder bed fusion. Opt Laser Technol. (2019)113.

[6] Vasileska E, Demir AG, Colosimo BM, Previtali B. Layer-Wise Control of Selective Laser Melting By Means of Inline Melt Pool Area Measurements.

[7] Criales LE, Arısoy YM, Lane B, Moylan S, Donmez A, Özel T. Laser powder bed fusion of nickel alloy 625: Experimental investigations of effects of process parameters on melt pool size and shape with spatter analysis. Int J Mach Tools Manuf. (2017)121(March):22–36.

[8] Hooper PA. Melt pool temperature and cooling rates in laser powder bed fusion. Addit Manuf. (2018).

[9] Furumoto T, Ueda T, Rizal M, Hosokawa A. Investigation of laser consolidation process for metal powder by two-color pyrometer and high-speed video camera. CIRP Ann - Manuf Technol. (2013)62(1):223–6.

[10] Thombansen U, Abels P. Observation of melting conditions in selective laser melting of metals (SLM). (2016)9741:97410S.

[11] Leung CLA, Marussi S, Atwood RC, Towrie M, Withers PJ, Lee PD. In situ X-ray imaging of defect and molten pool dynamics in laser additive manufacturing. Nat Commun. (2018)9(1):1–9.

[12] Parab ND, Escano LI, Fezzaa K, Everhart W, Rollett AD, Chen L, et al. Ultrafast X-ray imaging of laser – metal additive manufacturing processes research papers. (2018):1–11.

[13] Calta NP, Wang J, Kiss AM, Martin AA, Depond PJ, Guss GM, et al. An instrument for in situ time-resolved X-ray imaging and diffraction of laser powder bed fusion additive manufacturing processes. Rev Sci Instrum. (2018)89(5).

[14] Renwick RJ, Richardson RW. Experimental investigation of GTA weld pool oscillations. Weld J. (1983):29–35.

[15] Sorensen CD, Eagar TW. Digital Signal Processing As a Diagnostic Tool for Gas Tungsten Arc Welding. Adv Weld Sci &Technology. (1986):467–72.

[16] Maruo H, Hirata Y. Natural frequency and oscillation modes of weld pools. 1st report: Weld pool oscillation in full penetration welding of thin plate. Weld Int. (1993)7(8):614–9.

[17] Sorensen CD, Eagar TW. Modeling of oscillations in partially penetrated weld pools. J Dyn Syst Meas Control. (1990)112(3):469–74.

[18] Xiao YH, den Ouden G. A Study of GTA Weld Pool Oscillation. Weld J. (1990)(8):289-s to 293-s.

[19] Yoo CD, Richardson RW. Modeling of Weld Pool Oscillation using Energy Method. Q J Japan Weld Soc. (1994)12(1):30–8.

[20] Semak V V, Hopkins J a, McCay MH, McCay TD. Melt pool dynamics during laser welding. J Phys D Appl Phys. (1995)28(12):2443–50.

[21] Richter B, Blanke N, Werner C, Parab ND, Sun T, Vollertsen F, et al. High-speed X-ray investigation of melt dynamics during continuous-wave laser remelting of selective laser melted Co-Cr alloy. CIRP Ann. (2019).

[22] Caprio L, Demir AG, Previtali B. Comparative study between CW and PW emissions in selective laser melting. J Laser Appl. (2018)30(3):32305.

[23] Caprio L, Demir AG, Previtali B, Colosimo BM. Determining the feasible conditions for processing lunar regolith simulant via Laser Powder Bed Fusion. Addit Manuf. (2019):101029.

[24] Fabbro R. Melt pool and keyhole behaviour analysis for deep penetration laser welding. J Phys D Appl Phys. (2010)43(44).

[25] Carter GC, Nuttall AH. A brief summary of a generalized framework for power spectral estimation. Signal Processing. (1980)2(4):387–90.

[26] Haley CL, Anitescu M. Optimal Bandwidth for Multitaper Spectrum Estimation. IEEE Signal Process Lett. (2017)24(11):1696–700.

[27] Prerau MJ, Brown RE, Bianchi MT, Ellenbogen JM, Purdon PL. Sleep Neurophysiological Dynamics Through the Lens of Multitaper Spectral Analysis. Physiology. (2017)32(1):60–92.

[28] Klein T, Vicanek M, Simon G. Oscillations of the keyhole in penetration laser beam welding. J Phys D Appl

Phys. (1994)27(2):322–32.

[29] Scipioni Bertoli U, Guss G, Wu S, Matthews MJ, Schoenung JM. In-situ characterization of laser-powder interaction and cooling rates through high-speed imaging of powder bed fusion additive manufacturing. Mater Des. (2017)135:385–96.

[30] Mazzoleni L, Demir AG, Caprio L, Pacher M, Previtali B. Real-Time Observation of Melt Pool in Selective Laser Melting: Spatial, Temporal and Wavelength Resolution Criteria. IEEE Trans Instrum Meas. (2019).

[31] King WE, Barth HD, Castillo VM, Gallegos GF, Gibbs JW, Hahn DE, et al. Observation of keyhole-mode laser melting in laser powder-bed fusion additive manufacturing. J Mater Process Technol. (2014)214(12):2915–25.

[32] Semak V, Hopkins JA, Mccay MH. A technique for melt pool oscillation monitoring during laser spot welding. In: International Congress on Applications of Lasers & Electro-Optics. (1997.) p. C11--C20.

[33] Xiao YH, Den Ouden G. Weld pool oscillation during GTA welding of mild steel. Weld JOURNAL-NEW YORK-. (1993)72:428--s.

[34] Cunningham R, Zhao C, Parab N, Kantzos C, Pauza J, Fezzaa K, et al. Keyhole threshold and morphology in laser melting revealed by ultrahigh-speed x-ray imaging. Science (80-). (2019)363(6429):849–52.

[35] Trapp J, Rubenchik AM, Guss G, Matthews MJ. In situ absorptivity measurements of metallic powders during laser powder-bed fusion additive manufacturing. Appl Mater Today. (2017)9:341–9.

[36] Ye J, Khairallah SA, Rubenchik AM, Crumb MF, Guss G, Belak J, et al. Energy Coupling Mechanisms and Scaling Behavior Associated with Laser Powder Bed Fusion Additive Manufacturing. Adv Eng Mater. (2019)21(7):1–9.

[37] Zhou YH, Zhang ZH, Wang YP, Liu G, Zhou SY, Li YL, et al. Selective laser melting of typical metallic materials: An effective process prediction model developed by energy absorption and consumption analysis. Addit Manuf. (2019)25(October 2018):204–17.

[38] Mills KC. Recommended values of thermophysical properties for selected commercial alloys. Recommended Values of Thermophysical Properties for Selected Commercial Alloys. Woodhead Publishing; (2002.).

[39] Steen WM, Mazumder J. Laser Material Processing [Internet]. Vol. 1, Springer-Verlag London Limited. (2010.) 558 p.